

Iterative static field map estimation for off-resonance correction in non-Cartesian susceptibility weighted imaging

Guillaume Daval-Fr erot^{1,2,3} | Aur elien Massire¹ | Boris Mailhe⁴ |
Mariappan Nadar⁴ | Alexandre Vignaud²  | Philippe Ciuciu^{2,3}

¹Siemens Healthcare SAS, Saint-Denis, France

²CEA, NeuroSpin, CNRS, Universit  Paris-Saclay, Gif-sur-Yvette, France

³Inria, Palaiseau, France

⁴Siemens Healthineers, Digital Technology & Innovation, Princeton, New Jersey, USA

Correspondence

Philippe Ciuciu, NeuroSpin, CEA, Gif-sur-Yvette 91191, France.

Email: philippe.ciuciu@cea.fr

Purpose: Patient-induced inhomogeneities in the magnetic field cause distortions and blurring during acquisitions with long readouts such as in susceptibility-weighted imaging (SWI). Most correction methods require collecting an additional ΔB_0 field map to remove these artifacts.

Theory: The static ΔB_0 field map can be approximated with an acceptable error directly from a single echo acquisition in SWI. The main component of the observed phase is linearly related to ΔB_0 and the echo time (TE), and the relative impact of non- ΔB_0 terms becomes insignificant with TE >20 ms at 3 T for a well-tuned system.

Methods: The main step is to combine and unfold the multi-channel phase maps wrapped many times, and several competing algorithms are compared for this purpose. Four in vivo brain data sets collected using the recently proposed 3D spreading projection algorithm for rapid k-space sampling (SPARKLING) readouts are used to assess the proposed method.

Results: The estimated 3D field maps generated with a 0.6 mm isotropic spatial resolution provide overall similar off-resonance corrections compared to reference corrections based on an external ΔB_0 acquisitions, and even improved for 2 of 4 individuals. Although a small estimation error is expected, no aftermath was observed in the proposed corrections, whereas degradations were observed in the references.

Conclusion: A static ΔB_0 field map estimation method was proposed to take advantage of acquisitions with long echo times, and outperformed the reference technique based on an external field map. The difference can be attributed to an inherent robustness to mismatches between volumes and external ΔB_0 maps, and diverse other sources investigated.

KEYWORDS

ΔB_0 field map estimation, compressed sensing, non-Cartesian imaging, SPARKLING, SWI

1 INTRODUCTION

Susceptibility-weighted imaging (SWI)¹ is commonly used in high-resolution brain venography or traumatic brain injuries for its sensitivity to blood products and calcium.² The magnetic susceptibility of those compounds contributes to local field distortions visible on filtered phase maps. Long echo times TEs (e.g., TE \simeq 20 – 40 ms at 3 T) are typically used to enhance the susceptibility contribution, resulting in compromises on slice thickness to reach clinically acceptable scan times. Many parallel imaging and compressed-sensing (CS) methods^{3–9} have been proposed over the last 2 decades to accelerate MRI acquisitions and non-Cartesian sampling patterns^{10,11} have recently gained popularity. In particular, the trajectories based on the spreading projection algorithm for rapid k-space sampling (SPARKLING) in 2D¹¹ and 3D imaging^{12,13} can reach acceleration factor (AF) superior to 15 in scan times compared to fully sampled Cartesian imaging in high resolution (0.6 mm) isotropic brain imaging by taking advantage of all degrees of freedom offered by modern MR scanners and long observation windows (i.e., readouts).¹³ However, this experimental setting also results in off-resonance artifacts amplification that causes geometric distortions and image blurring.¹⁴ These artifacts are mainly caused by patient-induced static B_0 field inhomogeneities that are especially pronounced near air-tissue interfaces (e.g., close to the oral cavity and the ear canals). Non-Cartesian sampling patterns tend to be more sensitive to B_0 inhomogeneities causing local k-space inconsistencies over the different gradient directions.¹⁵ Therefore, specific attention must be paid to reduce signal and detail dropouts in these regions.

Different approaches exist to compensate for off-resonance artifacts during the acquisitions or later on in image reconstruction or post-processing. The default technique integrated in all scanners is the spherical harmonic shimming^{14,16} that allows the partial mitigation of patient-induced static inhomogeneities using a set of shim coils. A ΔB_0 field map is acquired and minimized with respect to the gradients that are expanded over a spherical harmonic basis (generally up to the second or third order). This calibration step is performed quickly using a low-resolution map because the technique does not allow precise correction.¹⁷ Although this approach provides a significant improvement on image quality, a complementary technique is required in the most demanding setups such as in EPI^{18,19} or in non-Cartesian imaging, that makes use of long readouts.^{12,13,20–22} Recent works have been proposed to improve this method using more efficient coil designs²³ that accurately fit the expected inhomogeneity profiles²⁴ using complementary data. Those experimental results

permit to achieve improved correction performances, but remain limited by the number of shimming coils to be deployed to reach the theoretical limits.²⁵ For that reason, alternative retrospective approaches are instrumental in correcting off-resonance effects once the k-space data has been collected.

In the particular case of Cartesian EPI, a well-known technique^{26,27} consists in inverting the gradient direction at every time frame to emphasize the geometric distortions and therefore, obtain a deformation map that can then be directly corrected. This technique is, however, difficult to transpose to non-Cartesian readouts (e.g., spirals, rosette, SPARKLING)^{11–13,20–22,28} because the gradient directions are strongly varying along multiple dimensions simultaneously. In such context, a more generic and well-established method^{29–33} consists in compensating the undesired ΔB_0 gradient by modifying the Fourier operator to integrate the prior knowledge of a ΔB_0 field map. This technique can be applied to both Cartesian and non-Cartesian data at the cost of much longer (e.g., 15-fold) image reconstruction times.

For multi-echo sequences, the ΔB_0 field map can be directly derived from the acquisitions.¹⁴ For single echo sequences, the constraint of knowing the ΔB_0 field map has been considered from different perspectives in the literature^{34–39} to avoid additional medium-to-high resolution multi-echo acquisitions that would counterbalance the goal of accelerating the original scan. A first solution is to integrate the multiple echoes into the desired sequences,^{40,41} however, they represent an additional constraint on the pulse sequence design that is not compatible with some protocols because of their long readouts. This holds in particular for multishot spiral,²² segmented EPI,¹⁸ or SPARKLING¹³ imaging. Post-processing approaches have been developed, notably by the teams that contributed to the correction method.^{34,35} One of the most popular approaches over the years initiated by Sutton et al³⁵ is to solve a non-convex optimization problem involving the ΔB_0 extended signal equation model during image reconstruction. Recent developments^{36,37} rely on tight regularizing constraints to make the solution locally smooth by projecting the gradients onto a set of functions (e.g., 2D Gaussians). Compared to the original implementation,³⁵ this approach guarantees a successful convergence to a local minimizer. However, the field maps shown in Patzig et al³⁷ are low resolution because of the involved smoothing constraints. Another possibility lies in the simulation of the ΔB_0 field map^{38,39} with mask-sensitive binary anatomy models, however, proposing an accurate mask is challenging without even considering the model limitations. Because the stated non-Cartesian SWI problem arises from long readouts centered over long TEs, in this paper, we propose to take advantage of the phase

properties in such context. Indeed the ΔB_0 contribution to the phase maps grows linearly with TE^{42} and becomes significantly dominating, whereas most other contributions remain constant or decay.^{14,43,44} The disproportion reaches a point where it can be assumed that the phase is equivalent to the ΔB_0 field map with minimal error.

In this work, a pipeline is proposed to convert the phase map extracted either from a spherical stack of 2D SPARKLING trajectories¹² or from full 3D SPARKLING ones¹³ into a high-resolution 3D ΔB_0 field map that is subsequently used to correct the SWI acquisition for B_0 inhomogeneities. These SPARKLING trajectories were specifically designed for SWI acquisitions with different acceleration factors [as defined later in Equation (10)]. The iterative procedure requires notably to address the problems of coil combination^{45–49} and phase unwrapping^{50–53} for which 2 and 4 algorithms, respectively, were jointly confronted. On 4 healthy volunteers at 3 T, the ΔB_0 field map estimates in the brain are directly compared to the individually matched acquired references and the benefit of this internal estimation is subsequently assessed on SWI brain images after offline image reconstruction.

2 THEORY

The simplest model⁵⁴ to recover a complex-valued MR image f from an acquired complex-valued signal s over time window T_{obs} at the grid position r from k-space trajectory k is:

$$f(r) = \int_{T_{\text{obs}}} s(t) e^{i2\pi k(t) \cdot r} dt. \quad (1)$$

The above equation corresponds to an adjoint Fourier transform of the raw data. However, this model does not account for the different perturbations of the signal s that occur during acquisition. A common extension that allows the recovery of a partially corrected image \hat{f} for the undesired effects of B_0 field inhomogeneities reads as follows:

$$\hat{f}(r) = \int_{T_{\text{obs}}} s(t) e^{i2\pi(k(t) \cdot r + \Delta B_0(r)t)} dt. \quad (2)$$

The additional gradient term within the exponential assumes the knowledge of the ΔB_0 field map. The most common method¹⁴ to find it relies on the measurements of phase maps. Indeed, the observed phase ϕ_{obs} of an MR image f at position r can be linked to the ΔB_0 field map as follows:

$$\phi_{\text{obs}}(r) \equiv \phi(r) \pmod{2\pi} \quad (3)$$

and

$$\phi(r) = \phi_{\Delta B_0}(r) + \phi_{\Delta B_1^\pm}(r) + \phi_{B_e}(r) + \phi_{\text{others}}(r), \quad (4)$$

where $\phi_{\Delta B_0}$, $\phi_{\Delta B_1^\pm}$, and ϕ_{B_e} are the phase contributions emanating from major sources: inhomogeneities in the B_0 and B_1 fields for the first 2 terms, and B_e field induced by eddy currents for the third one. The ϕ_{others} term includes the effect of minor sources such as heating and physiological motion. A common approximation is to consider ΔB_0 related to the TE through a linear relationship^{14,42}:

$$\phi_{\Delta B_0}(r, TE) = 2\pi TE \Delta B_0(r). \quad (5)$$

The common approach to estimate a ΔB_0 map is to perform acquisitions with multiple TE s,¹⁴ and consider other phase contributions as constant with respect to TE . For example, considering 2 TE s such that $TE_1 < TE_2$, we obtain:

$$\Delta B_0(r) = \frac{\phi(r, TE_2) - \phi(r, TE_1)}{2\pi(TE_2 - TE_1)}. \quad (6)$$

This formulation implies that ϕ must be recovered from ϕ_{obs} by solving Equation (3). Although many unwrapping algorithms have been proposed in the literature,^{50–53,55} convenient analytical choices are preferred to reduce the observed wrapping, and therefore, simplify or even avoid this step, such as applying a division over the complex-valued volumes acquired with close TE s.¹⁴ In contrast, our approach consists in taking advantage of acquisitions with long TE s to propose a high-resolution ΔB_0 map based on the phase image from a single echo SWI acquisition through the following approximation:

$$\Delta B_0(r) = \frac{\phi(r)}{2\pi TE}, \quad (7)$$

considering that other contributions are almost negligible for long TE s at high magnetic field for well-tuned MR scanners.^{45,56–59} Indeed the absolute error ε in the previous approximation can be decomposed into individually measurable contributions:

$$\varepsilon(r) = \left| \frac{\phi_{\Delta B_1^\pm}(r) + \phi_{B_e}(r) + \phi_{\text{others}}(r)}{2\pi TE} \right|. \quad (8)$$

The main component in Equation (8) is $\phi_{\Delta B_1^\pm}$ because it includes both the radiofrequency pulse inhomogeneities and the coil sensitivities. An optimal coil combination with respect to the signal-to-noise ratio can be computed when the coil sensitivity maps are known.⁴⁵ Similarly to the ΔB_0 map, these sensitivity maps require an additional acquisition and are therefore, usually unknown. Various methods exist to estimate them from the acquired multi-channel volume.^{45–47} After recombination, a constant phase shift ϕ_0 remains undetermined depending on

the reference coil.⁶⁰ This term can be simply removed if we assume that a 0-order B_0 shimming is applied and matches the acquisition box because no constant term is expected any longer. Both coil combination algorithms and 0-order B_0 shimming hypothesis are considered in later experiments.

The additional fields created by the radiofrequency pulse inhomogeneities and the eddy currents^{14,43,44} through the MR scanner and the coil are generally limited for well-designed and calibrated hardware.^{56,57} An experiment on oil phantom proposed in Supporting Information Section S1 suggests an error inferior to 2 Hz from the eddy currents contribution in the proposed experimental setup. However, the relative contribution of both sources increases with the B_0 field strength and may have a significant impact on the ΔB_0 estimation at very high magnetic fields.^{61,62} Overall, the related error at 3 T is expected to be inferior to 10 Hz^{45,56,57} on average, whereas off-resonance frequencies can reach up to 300 Hz.

Based on the literature, other sources such as heating⁵⁸ and physiological motion⁵⁹ can be neglected for static contributions. Note that the contribution from heating follows a similar relationship with respect to TE ⁵⁸ but is still considered negligible:

$$\phi_{\Delta T}(r, TE) = 2\pi TE \nu \alpha \Delta T(r), \quad (9)$$

where ν is the Larmor frequency and α the frequency shift per degree Celsius, whereas ΔT refers to the temperature variation at voxel r .

Stronger motion such as bulk motion during the sequence acquisition could greatly impede the estimation. This issue is considered to be addressed separately, because it would also hinder the overall quality of the images. Different methods exist to correct motion artifacts,^{63,64} however, the current clinical practice is to simply repeat the exam. Note that avoiding the ΔB_0 map acquisition already allows us to ignore potential inter-acquisitions mismatches caused by such motions. Overall, the main contributions to the estimation error ϵ are the radiofrequency pulse inhomogeneities, coils sensitivity, and eddy currents,^{56,57} along with an undetermined constant phase term supposedly close to 0.

Finally, the contribution from magnetic susceptibility of tissues has to be specifically preserved in the case of SWI. Indeed the susceptibility information, used to enhance diverse contrast sensitivities,² originates from minor B_0 inhomogeneities^{1,14} and therefore, the estimated ΔB_0 field map should exclude those contributions to avoid canceling them during the off-resonance correction. Because that information is usually extracted from high frequencies using filters,¹ similar filters can be used over

the ΔB_0 field map to remove this information from the correction step.

3 METHODS

Our contribution is 3-fold: first, different algorithms for coil combination and phase unwrapping is jointly studied. Second, the best combination is integrated into an iterative pipeline aiming to estimate the ΔB_0 field map. Third, this map is used to perform off-resonance corrections on the acquired k-space data. The performance of the later is evaluated by comparisons with corrections obtained from external ΔB_0 field maps.

3.1 Coil combination and phase unwrapping

A particular attention has been paid to the above-mentioned critical steps, namely the coil combination and phase unwrapping. Multiple algorithms have been jointly evaluated to reach an accurate and reliable estimation.

In regards to the coil combination, the technique developed by Parker et al⁴⁶ referred here to as virtual coil combination (VCC) appears as the state of the art among the phase-preserving techniques.⁶⁰ Another method introduced by Walsh et al,⁴⁷ referred here to as adaptive coil combination (ACC), has been improved contemporarily by Inati et al⁴⁸ to specifically preserve phase during combination. Both algorithms were internally implemented on graphical processing units (GPU) in Python⁶⁵ using the CuPy (<https://github.com/cupy/cupy>) module,⁶⁶ with specific modifications to the ACC method detailed in Supporting Information Section S2.

For phase unwrapping, 4 algorithms^{50–53} were considered to compare different approaches.⁶⁷ Only the method from Ghiglia et al⁵⁰ was implemented internally on GPU, with noticeable changes described in Supporting Information Section S3 to extend it to 3D imaging. The other approaches were tested on CPU thanks to different open-source implementations: scikit-image (<https://github.com/scikit-image/scikit-image>)⁶⁸ in Python for Herráez et al,⁵¹ the original implementation of ROMEO (<https://github.com/korbinian90/ROMEO>) in Julia⁶⁹ by Dymerska et al,⁵³ and PyMRT (<https://github.com/norok2/pymrt>)⁷⁰ in Python for Schofield et al.⁵² The method from Ghiglia et al⁵⁰ was the only one observed to benefit from masking the phase before application, so the others were not masked by default. Additionally, the method developed by Dymerska et al⁵³ was used along with the magnitude information, as recommended by the authors.

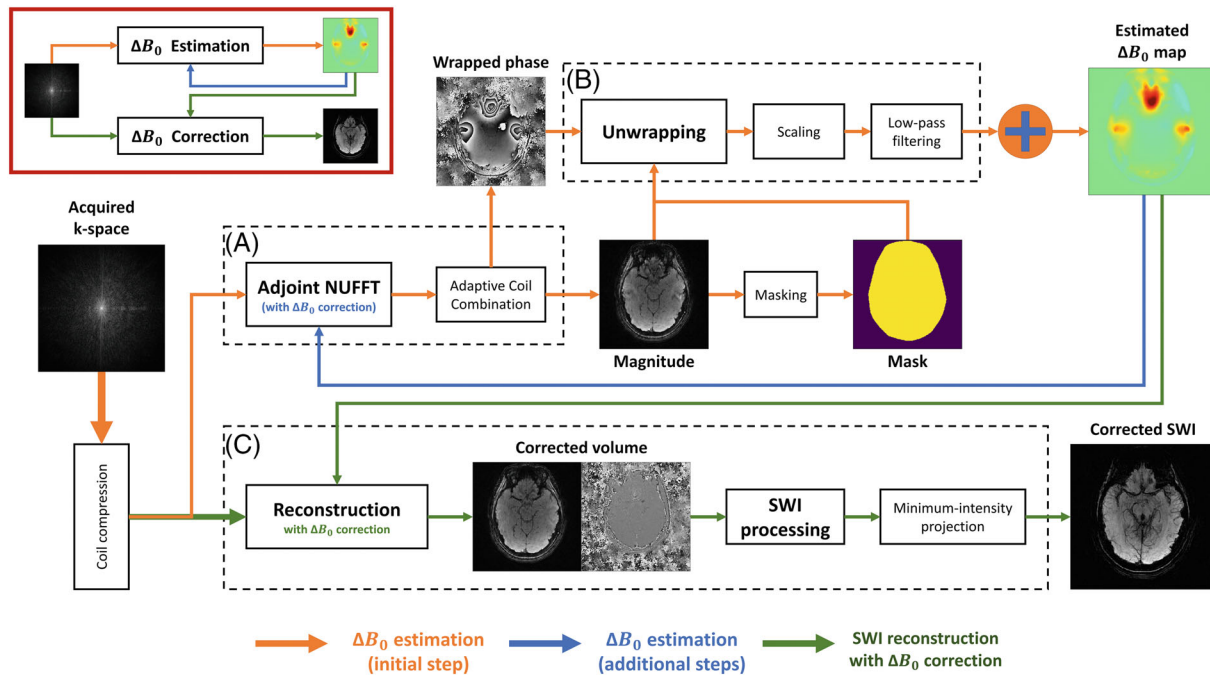


FIGURE 1 Pipeline for ΔB_0 iterative estimation followed by SWI reconstruction. The pipeline represents the overall process of ΔB_0 estimation (A,B) and the reconstruction with B_0 inhomogeneity correction (C). A simplified version is displayed in the upper left corner for clarification purpose. In block A, the undersampled acquired k-space is transformed into a complex-valued volume, and then converted in block B into the required ΔB_0 field map. Blocks A and B can be looped over for a few iterations to ensure a robust estimation (blue arrows) by adding residual estimations from each step (orange-circled blue plus sign). The produced field map is then used along with the undersampled k-space in block C to obtain the corrected SWI volume

A qualitative evaluation of the estimated maps by visual inspection after 1 iteration was performed over 4 volumes. The main criterion was to avoid anomalies in the ΔB_0 regions and outside the skull where the phase is locally inconsistent because of a void signal. The second criterion was to obtain off-resonance values as close as possible to the acquired ΔB_0 map used as reference.

3.2 ΔB_0 field map estimation

The ΔB_0 map estimation pipeline is represented in Figure 1. First, the non-Cartesian multi-coil k-space data was compressed using the principal component analysis-based method proposed by Buehrer et al.⁷¹ The channel dimension is reduced to 30 components for image reconstruction, and to 5 components for the ΔB_0 map estimation. An adjoint non-uniform fast Fourier transform (NUFFT)⁷² with a pre-computed density compensation⁷³ was then applied to the 5 compressed channels to produce multi-channel complex-valued volumes. The different channels were combined using the ACC method⁴⁷ and the resulting magnitude image was used to produce a brain mask, and then combined with magnitude and phase images.

At this stage, the observed phase ϕ_{obs} remains wrapped over the $(-\pi, \pi]$ domain. Phase unwrapping was performed using the algorithm proposed in Ghiglia and Romero,⁵⁰ which consists in solving a Poisson equation weighted by the previously computed magnitude image. Finally, the phase maps were scaled by $1/2\pi TE$ following Equation (7) and a low-pass filter was applied using a Hanning window over the central third of the Fourier domain. This filtering step is specific to SWI and is carried out to preserve the susceptibility contributions in the high frequencies during the ΔB_0 correction. This point is detailed in Supporting Information Section S6. Other contrasts relying on phase information might also require specific ΔB_0 map processing.

Therefore, a first estimation of the ΔB_0 map is computed. For highly accelerated acquisitions (e.g., $AF > 15$ as defined below in Equation [10]), the signal-to-noise ratio in the ΔB_0 regions can be too low to provide an accurate field map. Therefore, the process should be iterated to improve the first estimation as shown in Figure 1. In the next iterations, the regular NUFFT operator is replaced by a correcting pseudo-NUFFT operator,³² combined with the previous ΔB_0 estimation. This step actually consists of interpolating the usually intractable gradient compensation through a weighted sum of

regular NUFFT operators. The histogram-based coefficients were used as weights with a number of interpolators $L = \lceil (\Delta B_{0\max} - \Delta B_{0\min}) / 25 \rceil$ to maintain an approximation root-mean-square error (RMSE) below 10^{-5} . This way, some signal is recovered in regions where some of the inhomogeneities are being removed. The updated ΔB_0 map estimate provides information about previously missed inhomogeneities, and is added to the previous one(s) until convergence. Hence, the resulting map is also corrected for geometric distortions caused by B_0 inhomogeneities. In the following experiments, 3 additional iterations were run to reach convergence, based on experiments available in Supporting Information Section S5.

3.3 Data acquisition and reconstruction

A total of 4 SWI volumes were acquired with non-Cartesian 3D gradient echo sequences, each on a different healthy volunteer at 3 T (Magnetom Prisma^{FIT}, Siemens Healthcare, Erlangen, Germany) with a 64-channel head/neck coil array. Local and national ethical committees have approved the protocol, and written consent was obtained from the volunteers. Two different sampling patterns were used with distinct acceleration factors defined as:

$$AF = \frac{N \times N_z}{N_c}, \quad (10)$$

with N the in-plane resolution, N_z the number of slices and N_c the number of spokes. The recently proposed 3D spherical stack of SPARKLING¹² was used for 2 volumes (referred to as 1 and 2) with $AF = 10$, and its recent extension, namely full 3D SPARKLING,¹³ was considered for the other 2 (referred to as 3 and 4) with $AF = 20$. All acquisitions were performed with the following parameters: a 0.6 mm isotropic resolution, a field-of-view of 24 cm in-plane ($N = 384$) over 12.5 cm ($N_z = 208$), an observation time of $T_{\text{obs}} = 20.48$ ms centered around an $TE = 20$ ms, a repetition time $TR = 37$ ms. For the spherical stack of SPARKLING acquisitions (1, 2), we used a dwell time $\Delta t = 5$ μs , and a number of spokes $N_c = 8192$ that resulted in an acquisition time of 5 min. For the full 3D SPARKLING (3, 4), a smaller dwell time $\Delta t = 2$ μs was used to balance the smaller number of spokes $N_c = 4096$ that resulted in a shorter acquisition of 2 min 30 s. For comparison purposes, an additional reference ΔB_0 map was acquired with a 2D gradient echo sequence using the following parameters: an acquisition time of 2 min 43 s (no acceleration), same field-of-view, a 2 mm isotropic resolution, $2 TE_1 = 4.92$ ms and $TE_2 = 7.38$ ms. Those TEs allow for an excursion of ± 203 Hz, resulting in 1 phase wrap present in all

references and unwrapped using the method proposed by Herráez et al.⁵¹

MR image reconstruction was performed offline using the pysap-mri (<https://github.com/CEA-COSMIC/pysap-mri>) software,^{74,75} (Figure 1C) which implements 3D self-calibrated compressed sensing reconstruction (ℓ_1 -norm regularization in the wavelet domain uses symlet 8 and 3 scales of decomposition).⁷⁶ The ΔB_0 correction was performed using the approximation described in Fessler et al.,³² with the number of interpolators L chosen as mentioned previously. Overall, the volumes were reconstructed considering 3 competing strategies: without correction, with correction based on the acquired ΔB_0 field map used as a reference, and with correction based on the estimated ΔB_0 field map. Further details about the offline reconstruction and correction are given in Supporting Information Section S4.

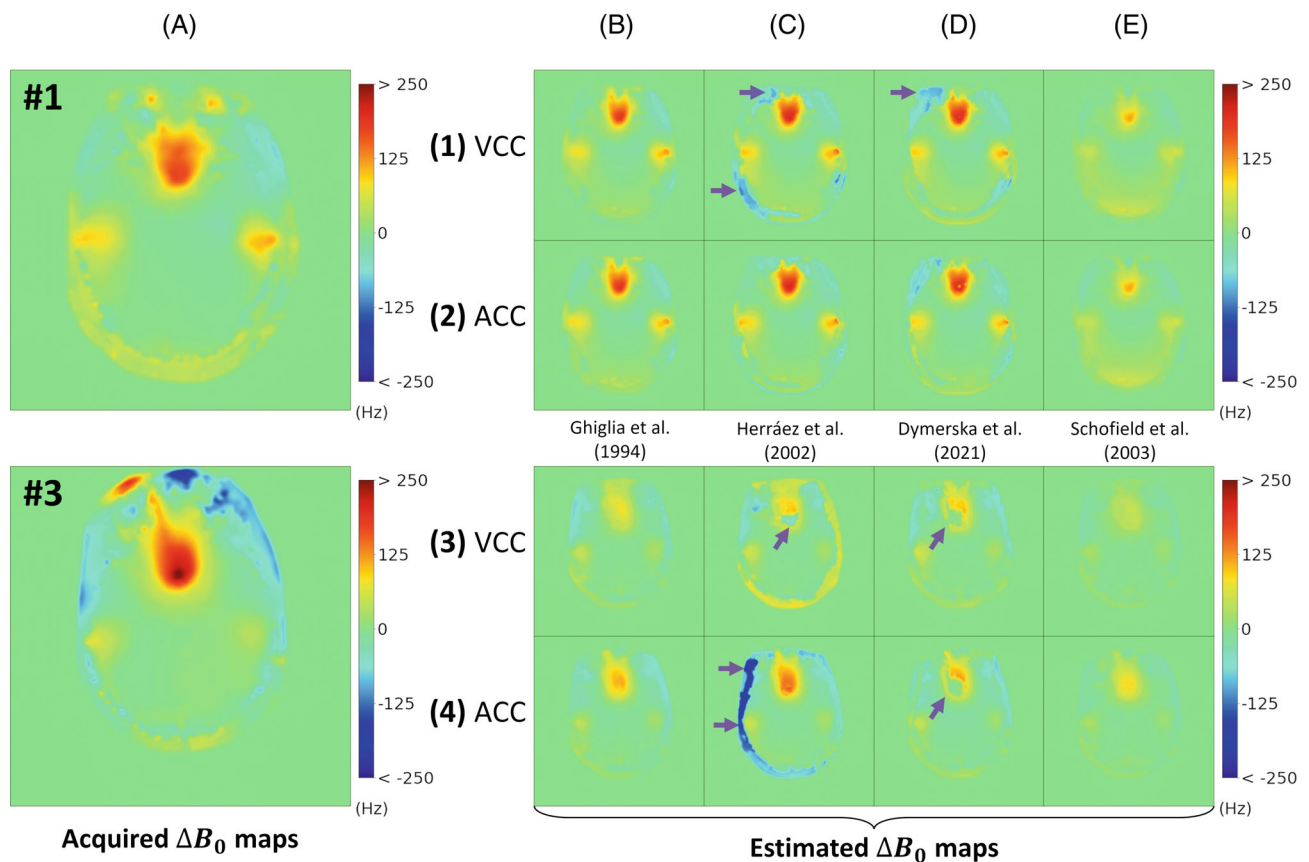
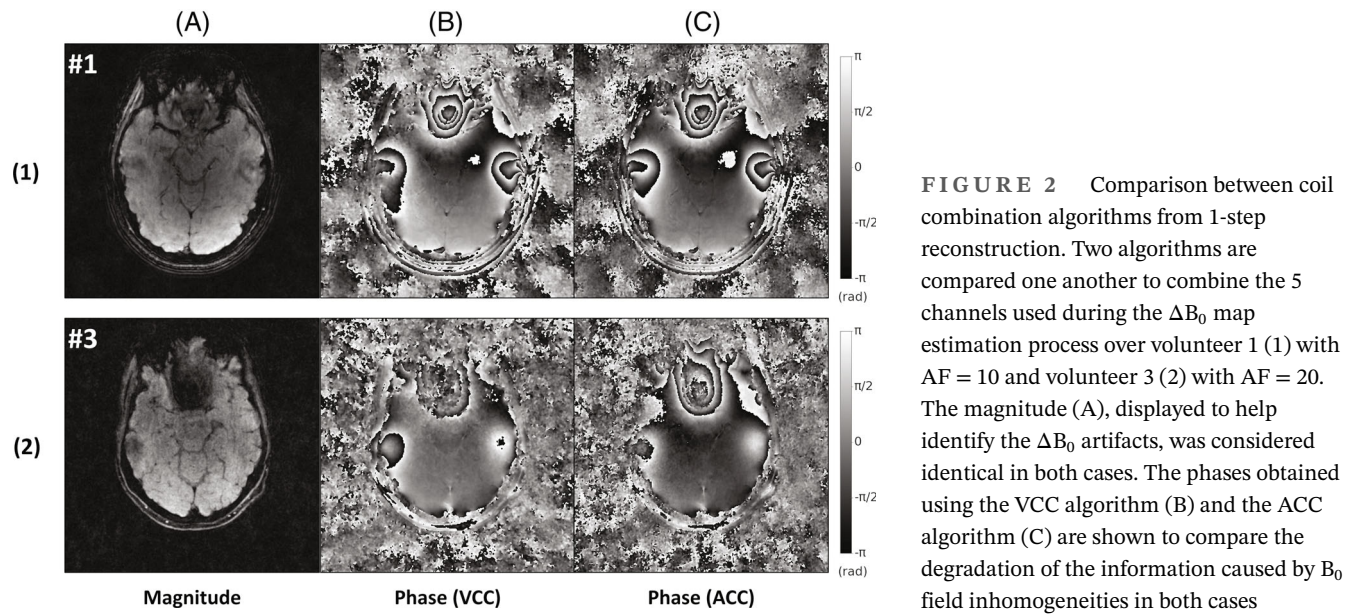
Finally, SWI specific processing as described in Haake et al.¹ was applied. The low frequencies were extracted by applying a Hanning window over the central third of the k-space, before being removed from the phase image to obtain a high frequency map, subsequently normalized to produce a continuous mask. The magnitude image was multiplied 5 times by the mask, and a minimum-intensity projection (mIP) was computed using a thickness of 8 mm. All post-processing was run on a 2560 cores Quadro P5000 GPU and 16 GB of GDDR5 VRAM (NVIDIA, Santa Clara, California, USA).

4 RESULTS

4.1 Coil combination and phase unwrapping

Different algorithms were considered in the estimation pipeline for the coil combination and unwrapping tasks, and results are shown in Figures 2 and 3, respectively. The 2 coil combination algorithms compared in Figure 2, namely VCC (Figure 2B) and ACC (Figure 2C), obtain similar performances for $AF = 10$ (row 1), whereas an overall degradation can be observed at $AF = 20$ (row 2). The front region close to the sinuses in (Figure 2B2) with VCC is dominated by noise, making difficult to estimate even visually the unwrapped phase values. On the other hand, the ACC method produces locally consistent results (Figure 2C2) with only some blurring in the regions associated with the highest off-resonance frequencies, therefore, obtaining more reliable phase maps.

The phase maps from Figure 2 are then unwrapped using different algorithms and processed to yield the estimates shown in Figure 3, respectively, using VCC (rows 1,3) and ACC (rows 2,4) methods on both volunteers 1 (rows 1,2) and 3 (rows 3,4). Most unwrapping algorithms



are consistent with the reference at $AF = 10$ (rows 1,2) except for Schofield et al's⁵² method (Figure 3E). However at $AF = 20$ (rows 3,4), no unwrapping algorithm managed to obtain results close to the reference maps in 1 step. Particularly, frequency values seem to drop significantly in key regions pointed on (Figure 3C3) and (Figure 3D3-4), using respectively, Herráez et al's⁵¹ and Dymerska et al's⁵³ methods. Such behavior can be detrimental to the additional iteration steps. For the other algorithms the field map remains locally smooth, however, its values are underestimated as illustrated in Figure 3B4,C4. An improved estimation is achieved in the inner region in Figure 3C4 with the method proposed by Herráez et al,⁵¹ balanced by extreme frequencies outside the skull on the left side, also observed in Figure 3C1,D1. Overall, the approach proposed by Ghiglia et al,⁵⁰ shown in Figure 3B, is preferred because of the absence of detrimental patterns, particularly when combined with the ACC method^{47,48} shown in rows (2,4).

4.2 ΔB_0 field map estimation

The first estimation step described previously took ~ 40 s to compute on average, with the following details: adjoint NUFFT computation in 16 s, coil combination in 5 s, phase unwrapping in 8 s, and masking, filtering, and scaling in 11 s. Additional steps may last between 3 and 5 min depending on the number of interpolators L used for correction, which tends to increase at each step. Note that the ΔB_0 correcting pseudo-NUFFT operator³² can be parallelized with more resources to achieve a duration for additional steps close to 40 s as well. Overall, the estimation time contributes marginally to the 6 to 8 h required to perform the state-of-the-art correction.³²

The intermediate estimation steps are represented in Figure 4. For both volumes, the low-frequency phase is progressively canceled over the iterations, whereas the ΔB_0 map converges. The resulting ΔB_0 maps are shown for all volumes in Figure 5 along with the acquired reference maps. The phase images obtained after 1 correction step with the acquired maps are shown on Figure 5 row 4. For each volume, an important phase component remains, particularly in the bucco-nasal regions. This observed phase is wrapped from negative to positive values, almost reaching an entire 2π cycle that corresponds to an inappropriate over-correction of 50 Hz [Equation (5)]. A remaining phase component from other sources is indeed expected in Equation (4), but those regions are specifically associated with B_0 inhomogeneities and the values are too large to correspond to ΔB_1 or B_e contributions. On the other hand, the estimated maps produce spatially homogeneous phase images (see row 6 in Figure 5).

More details are available in Supporting Information Section S7.

A comparison between the estimated and acquired ΔB_0 maps is proposed for all volumes in Figure 6. As shown in the superimposed histograms, the estimated frequencies tend to be lower than the acquired ones, therefore, confirming that references might be over-estimated as observed in Figure 5. Additionally, this is quantitatively assessed through the linear regression slopes around 0.9. The distributions are, however, similar as shown by the Pearson correlation coefficients $R \geq 0.93$. The RMSE varies from 6.69 Hz for the first volume to 10.80 Hz for the third volume. A noticeable shift of 7.27 Hz is observed for the third volume (originating from the acquired map) although it has the highest R value.

A global specific absorption rate (SAR) of 3% was measured during examinations. Considering a homogeneous temperature rise, the heating contribution to the phase can be roughly estimated around 5 mHz using Equation (9) (with $\nu = 127.74$ MHz, $\alpha = -0.01$ ppm/ $^{\circ}$ C). This confirms that the temperature contribution to the phase variation can be neglected for the proposed sequence.

4.3 ΔB_0 artifacts correction

The volumes with SWI processing are displayed in Figure 7 for $AF = 10$ and Figure 8 for $AF = 20$ with emphasis on the bucco-nasal region. Overall, the less affected volume by the correction is 2, whereas the more impacted is 1. This striking difference cannot be explained by acquisition parameters, which were similar for both. Besides the main artifact, the shape of the anterior region for volume 1 has indeed become sharper. Stronger artifacts are observed in volumes 3 and 4 along with a larger correction. Quantitative comparisons are available in Supporting Information Section S7. Overall, the corrections are improving the image quality for all volumes, although some regions cannot be recovered.

Although the corrections obtained with the reference and proposed ΔB_0 maps are similar, some noticeable differences persist. On volume 1 (Figure 7A), the right part of the brain visible on the axial and coronal views (Figure 7A2) suffers from degradation only present in the reference correction using the external map. The anterior region previously mentioned recovers a wider area shown with dotted lines when using the estimated map. Almost no difference is visible between the 2 corrections on volumes 2 and 4 except when comparing the axial slices (Figure 7B,C). Finally, both volumes 1 and 3 demonstrate a definite advantage of using the proposed ΔB_0 field map estimation technique compared to using the external ΔB_0 field map.

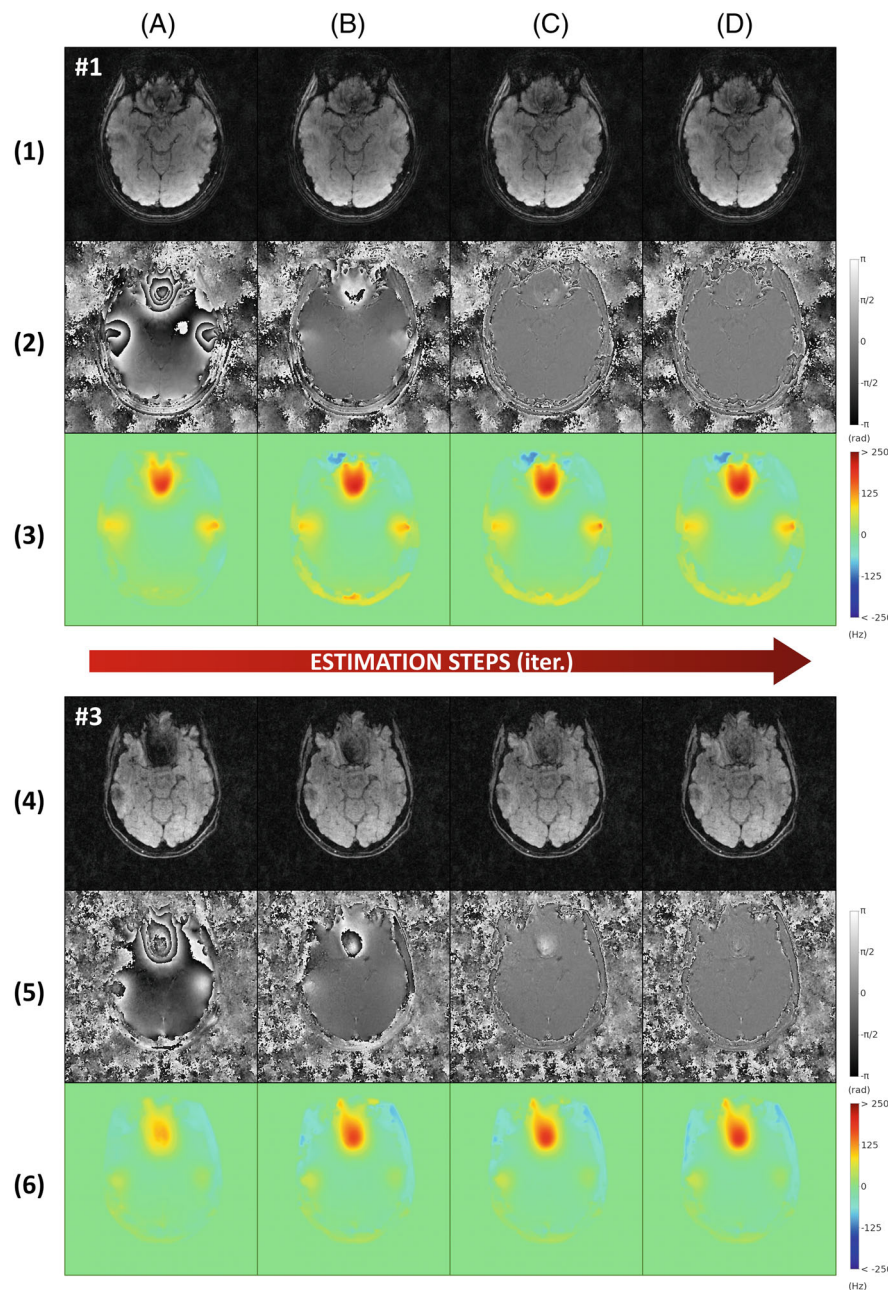


FIGURE 4 Iterative estimations using the selected pipeline. The 4-iteration estimation process is illustrated from columns (A) to (D) over 2 volumes to show the evolution of their ΔB_0 map estimates: top rows (1-3) are obtained from volunteer 1 with $AF = 10$, and bottom rows (4-6) are obtained from volunteer 3 with $AF = 20$. Rows 1 and 4 correspond to the magnitude images, rows 2 and 5 to the wrapped phase images, and rows 3 and 6 to the iterative estimated ΔB_0 field maps obtained from (1,2) and (4,5), respectively

5 DISCUSSION

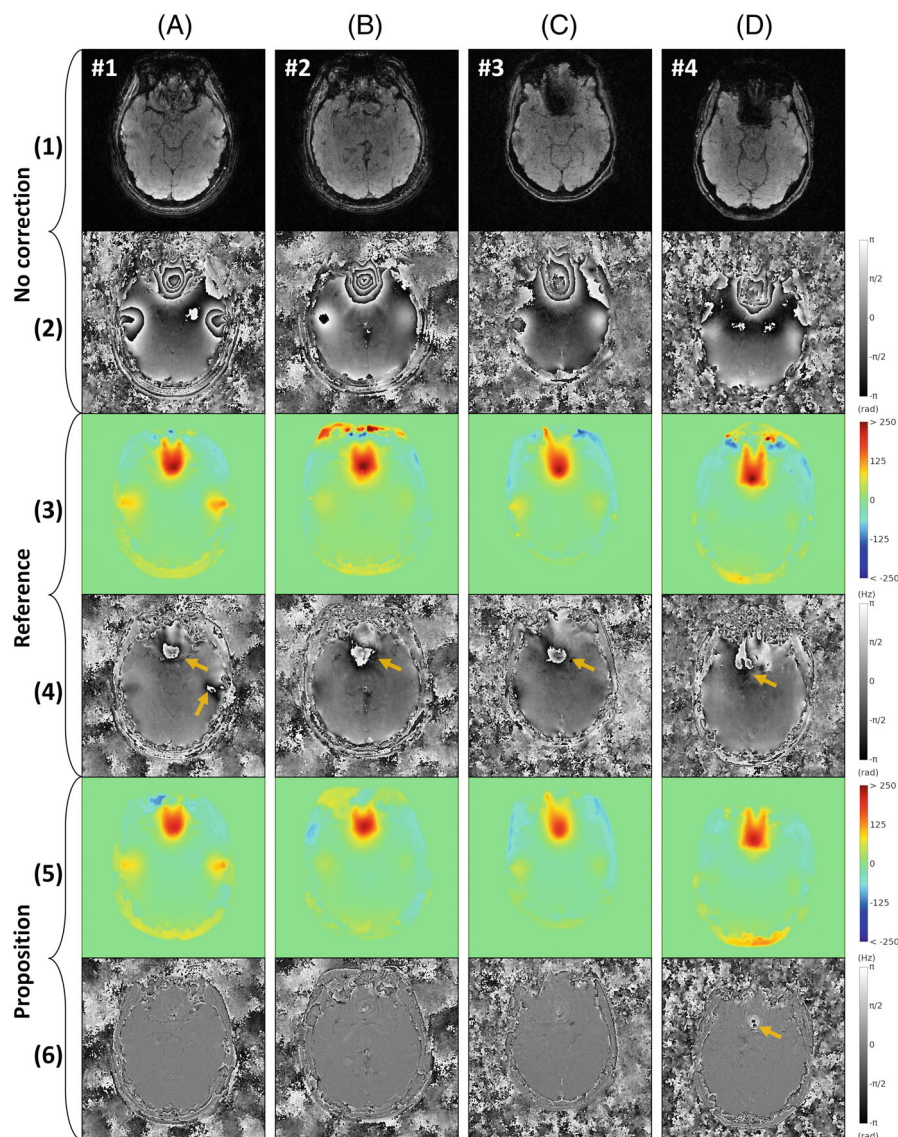
An iterative pipeline was established by comparing 2-coil combination and 4 phase unwrapping algorithms to produce a robust ΔB_0 field map estimate. The coil combination method from Walsh et al,⁴⁷ further improved by Inati et al,⁴⁸ along with the phase unwrapping method developed by Ghiglia et al⁵⁰ and embedded in an iterative pipeline permit to obtain a stable ΔB_0 estimation that empirically converged in few iterations. The resulting maps were observed to be highly correlated with the acquired maps used as reference. Improved corrections were generally observed with the proposed method over

the references, whereas none of the expected sources of error seemed to impact the correction.

5.1 ΔB_0 field map estimation

The differences observed between the acquired and estimated ΔB_0 maps have a few distinct causes. The first one to consider is the quality of the acquired ΔB_0 map. The number of TEs and their proximity in time can influence the measurements¹⁴ and therefore, the computation of the ΔB_0 map using Equation (6). Although 2 close echoes facilitate the phase unwrapping task, as

FIGURE 5 Comparison of the ΔB_0 field maps and the resulting phase images. All 4 volumes are displayed from left to right in columns (A) to (D), respectively. Rows 1 and 2 correspond to the uncorrected magnitude and phase images, row 3 corresponds to the acquired ΔB_0 field maps used to produce the corrected phase images (row 4) after 1 iteration, and row 5 corresponds to the estimated ΔB_0 field maps used to produce the corrected phase images (row 6) after 1 iteration



mentioned in the Theory section, a third and more distant echo can be used to strengthen the linear regression for peak values, which might otherwise be less accurate.^{14,24} The residual phase shown in Figure 5D suggests an over-correction and hence, that the acquired ΔB_0 field maps are all over-evaluated. Therefore, the difference observed between acquired and estimated ΔB_0 field maps should be considered carefully. Additionally, a mismatch between the external and estimated field maps could also be caused by inter-scan motion, but it would not explain the overall lower values in the proposed estimation. The resolution was also suspected to impact the correction,⁷⁷ but experiments proposed in Supporting Information Section S6 showed almost no difference when downsampling the ΔB_0 map estimates. Overall, the external ΔB_0 field maps could be improved to provide a better quality assessment of the ΔB_0 map estimation algorithm.

The second element to take into account is the modeling error ε involved in Equation (8). Besides the contributions from the ΔB_1 and B_e fields, the hypothesis of zero-order B_0 shimming stated in the Theory section was not systematically respected. Indeed, as observed in Figure 6, the linear regressions yield non-null constant frequency shifts. For 3 volumes, a variation of <2 Hz is observed, whereas almost 8 Hz are reached with volume 3. However, this difference does not seem to imbalance the correction, because this volume still presents clear improvements using the proposed estimation over the reference.

Finally, the last possible explanation for the observed difference is the methods used in the estimation pipeline. The strongly accelerated acquisitions ($AF = 20$) showed phase degradation near the bucco-nasal region, but still converged to a similar quality of ΔB_0 map estimates as those obtained at $AF = 10$. However, as pointed out in

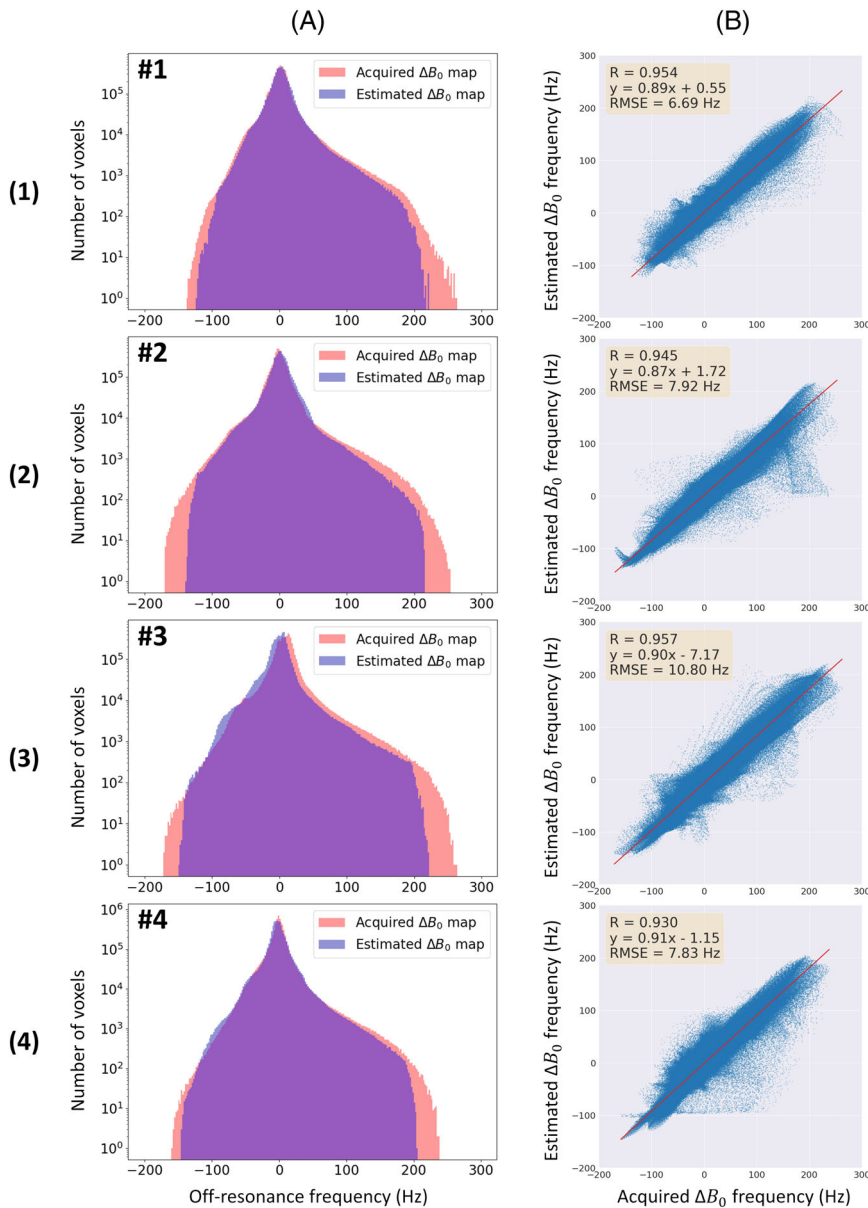


FIGURE 6 Comparison between acquired and estimated ΔB_0 maps. The acquired and estimated ΔB_0 field maps are confronted one another through superimposed histograms (A) and linear regressions (B) over the spherical stacks of SPARKLING acquisitions (1,2) with AF = 10 and the full 3D SPARKLING acquisitions (3,4) with AF = 20

Robinson et al,⁶⁰ the selected method by Ghiglia et al⁵⁰ is a non-exact method that removes some spatial components of the phase. It could cause the lower estimated frequencies observed in Figure 6, but would not explain that phase residuals are present in the references rather than in the proposed correction in Figure 5. An iterative solution allowed us to favor the robustness of the unwrapping algorithm over its accuracy, but methods that are more recent could be explored to obtain a better compromise in fewer iterations.^{60,78}

5.2 ΔB_0 artifacts correction

In terms of image quality, 2 volumes (1, 3) under study showed a clear advantage in using the proposed method.

In contrast, for the other 2 (2, 4), almost no difference was observed with the references (Figures 7 and 8). Volume 4 represents the worst estimation case, because it also has the lowest correlation coefficient between the acquired and estimated ΔB_0 maps (Figure 6). On volume 1, the degradation brought by the reference correction on the right side of the brain (Figure 7A2) could be explained by unexpected inter-scan movements causing a mismatch between the map and the SWI volume. The proposed method overcomes such issue as the ΔB_0 map is internally extracted from the same data set. Besides the partial correction with both the acquired and estimated ΔB_0 maps, no spatial degradation that could be attributed to the pipeline or the ΔB_1 and B_e fields has been observed. The above-mentioned sources of error seem less impactful than the gain issuing

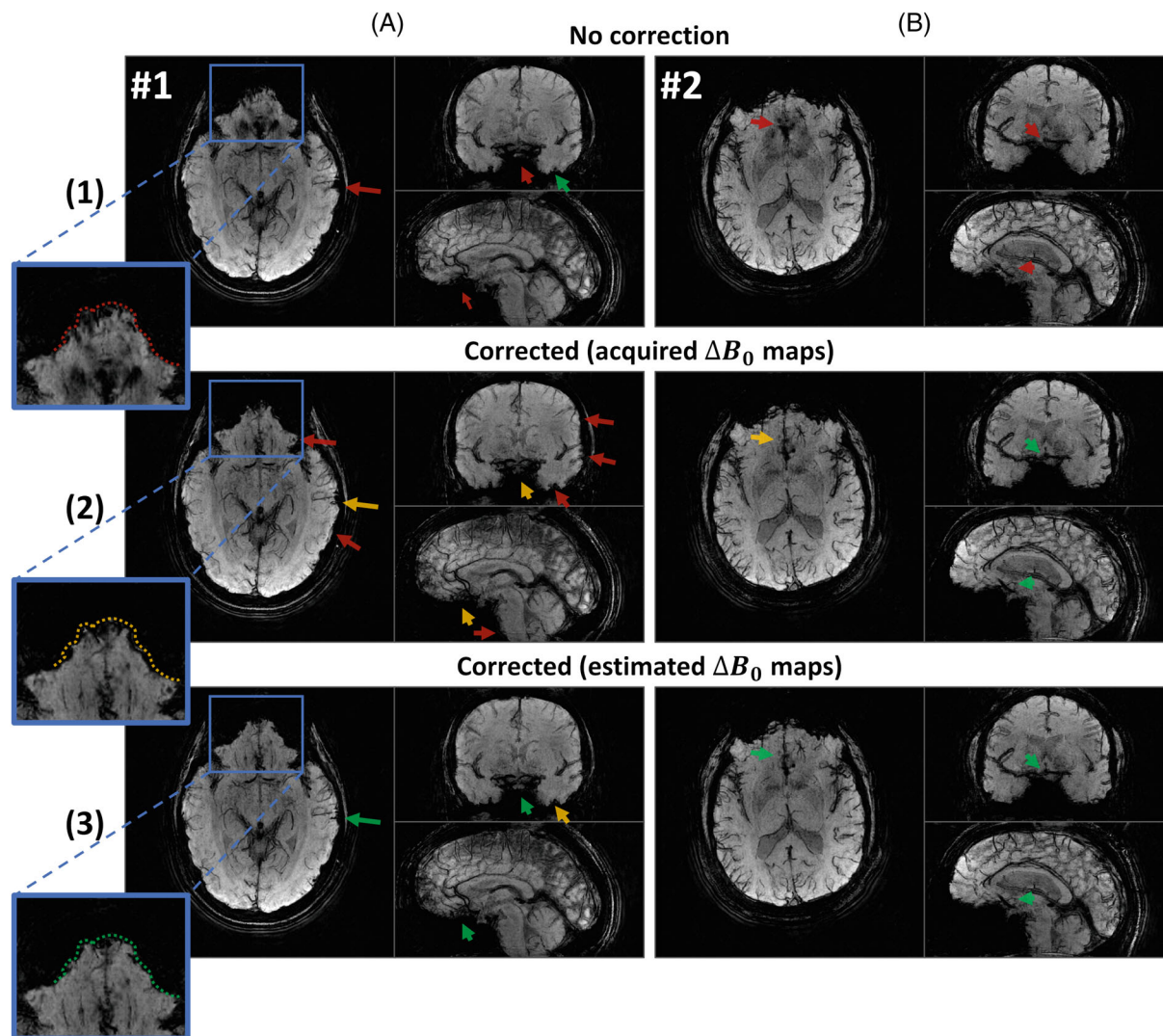


FIGURE 7 Comparison of ΔB_0 correction with acquired and estimated maps for $AF = 10$. The different volumes obtained from the spherical stack of SPARKLING acquisitions on volunteers 1 and 2 with $AF = 10$, SWI processing and a 8 mm minimum intensity projection (mIP) are displayed on the left column (A) and right column (B), respectively, according to the following conventions: without ΔB_0 correction in row 1, corrected using acquired ΔB_0 field maps in row 2, corrected using the estimated ΔB_0 field maps in row 3. Different artifact and correction details are pointed out using the following color-coded arrows: artifacted (red), mitigated (orange), and corrected (green). The dotted lines overlaid to the frontal lobe in the axial views of column 1 are used to project the edges from (A1) onto (A2) and (B3) for comparison purpose

from high resolution, robustness to motion, and reduced acquisition time.

6 CONCLUSIONS

MR imaging contrasts based on long readouts tend to suffer from B_0 inhomogeneities and therefore, from signal dropout, especially in non-Cartesian acquisitions used to reach shorter scan times. Moreover, long TEs such as in SWI facilitate the estimation of a ΔB_0 field map that can be further used for artifact correction as proposed in this

paper. The proposed approach actually relies on the internal phase measurements during SWI acquisition and on some tenable assumptions concerning its main contributions to produce a high resolution and robust-to-motion ΔB_0 field map in a few minutes only. This approach can be used a posteriori during the image reconstruction step and can deliver equivalent to improved corrections compared to the reference, which requires itself additional scan time. The estimation duration could be reduced in the future by improving the different pipeline steps with more advanced coil combination or phase unwrapping algorithms. Last, future work could focus on integrating optimization-based

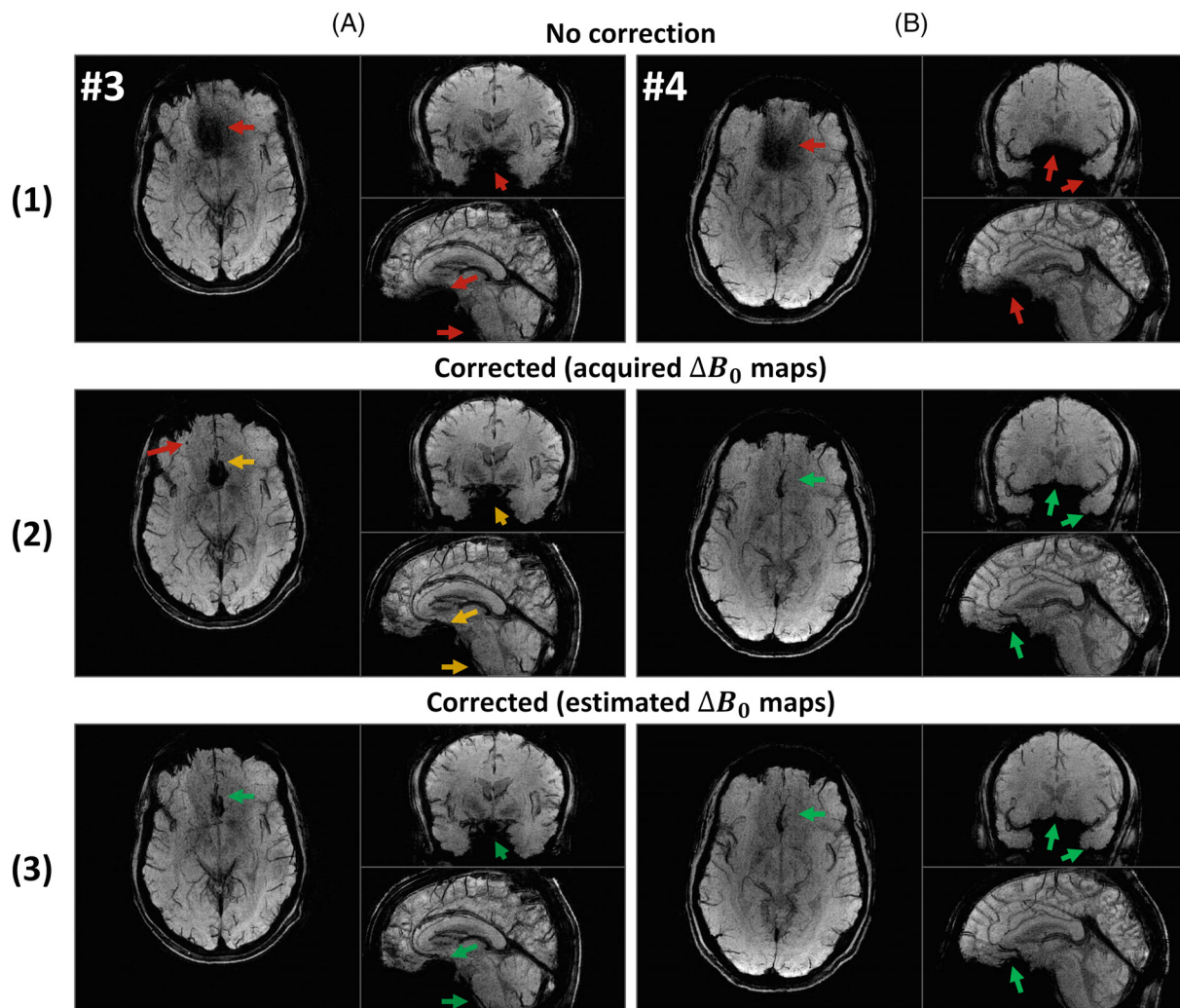


FIGURE 8 Comparison of ΔB_0 correction with acquired and estimated maps for $AF = 20$. The different volumes obtained from the full 3D SPARKLING acquisitions on volunteers 3 and 4 with $AF = 20$, SWI processing and a 8 mm minimum intensity projection (mIP) are displayed on the left column (A) and right column (B), respectively, according to the following conventions: without ΔB_0 correction in row (1), corrected using acquired ΔB_0 field maps in row 2, corrected using the estimated ΔB_0 field maps in row (3). Different artifact and correction details are pointed out using the following color-coded arrows: artifacted (red), mitigated (orange), and corrected (green)

estimation methods to account for bulk motion, or on extending this work from static imaging to EPI, similarly to recent works by Dymerska et al.¹⁹

ACKNOWLEDGMENTS

The concepts and information presented in this article are based on research results that are not commercially available. Future availability cannot be guaranteed. We thank Chaithya Giliyar Radhakrishna for his numerous technical contributions, and Dr. Caroline Le Ster and Dr. Alexis Amadon for useful discussions.

CONFLICT OF INTEREST

Guillaume Daval-Fr erot, Aur elien Massire, Boris Mailhe and Mariappan Nadar are all employed by Siemens Healthcare.

ORCID

Alexandre Vignaud  <https://orcid.org/0000-0001-9203-0247>

REFERENCES

- Haacke EM, Xu Y, Cheng Y-CN, Reichenbach JR. Susceptibility weighted imaging (SWI). *Magn Reson Med*. 2004;52:612-618.
- Wu Z, Mittal S, Kish K, Yu Y, Hu J, Haacke EM. Identification of calcification with MRI using susceptibility-weighted imaging: a case study. *J Magn Reson Imaging*. 2009;29:177-182.
- Pruessmann KP, Weiger M, B ornert P, Boesiger P. Advances in sensitivity encoding with arbitrary k-space trajectories. *Magn Reson Med*. 2001;46:638-651.
- Griswold MA, others. Generalized autocalibrating partially parallel acquisitions (GRAPPA). *Magn Reson Med*. 2002;47:1202-1210.

5. Lustig M, others. Sparse MRI: the application of compressed sensing for rapid MR imaging. *Magn Reson Med*. 2007;58:1182-1195.
6. Seiberlich N, Breuer FA, Blaimer M, Barkauskas K, Jakob PM, Griswold MA. Non-Cartesian data reconstruction using GRAPPA operator gridding (GROG). *Magn Reson Med*. 2007;58:1257-1265.
7. Vasanawala SS, Alley MT, Hargreaves BA, Barth RA, Pauly JM, Lustig M. Improved pediatric MR imaging with compressed sensing. *Radiology*. 2010;256:607-616.
8. Boyer C, others. On the generation of sampling schemes for MRI. *SIAM Imaging Sci*. 2016;9:2039-2072.
9. Luo T, Noll DC, Fessler JA, Nielsen J-F. A GRAPPA algorithm for arbitrary 2D/3D non-Cartesian sampling trajectories with rapid calibration. *Magn Reson Med*. 2019;82:1101-1112.
10. Polak D, Cauley S, Huang SY, et al. Highly-accelerated volumetric brain examination using optimized wave-CAIPI encoding. *J Magn Reson Imaging*. 2019;50:961-974.
11. Lazarus C, Weiss P, Chauffert N, et al. SPARKLING: variable-density k-space filling curves for accelerated T2*-weighted mri. *Magn Reson Med*. 2019;81:3643-3661.
12. Lazarus C, Weiss P, El Gueddari L, et al. 3D variable-density SPARKLING trajectories for high-resolution T2*-weighted magnetic resonance imaging. *NMR Biomed*. 2020;33:e4349.
13. Chaithya G, Weiss P, Massire A, Vignaud A, Ciuciu P. Optimizing full 3D SPARKLING trajectories for high-resolution T2*-weighted magnetic resonance imaging.; 2021.
14. de Graaf RA, Juchem C. B0 shimming technology. *Magnetic Resonance Technology: Hardware and System Component Design*; Royal Society of Chemistry; 2016:166-207.
15. Yudilevich E, Stark H. Spiral sampling in magnetic resonance imaging-the effect of inhomogeneities. *IEEE Trans Med Imaging*. 1987;6:337-345.
16. Gruetter R. Automatic, localized in vivo adjustment of all first-and second-order shim coils. *Magn Reson Med*. 1993;29:804-811.
17. Wachowicz K. Evaluation of active and passive shimming in magnetic resonance imaging. *Res Rep Nucl Med*. 2014;4:1-12.
18. Sati P, Thomasson D, Li N, et al. Rapid, high-resolution, whole-brain, susceptibility-based MRI of multiple sclerosis. *Mult Scler J*. 2014;20:1464-1470.
19. Dymerska B, Poser BA, Barth M, Trattng S, Robinson SD. A method for the dynamic correction of B0-related distortions in single-echo EPI at 7 T. *Neuroimage*. 2018;168:321-331.
20. Weiger M, Pruessmann KP, Österbauer R, Börner P, Boesiger P, Jezzard P. Sensitivity-encoded single-shot spiral imaging for reduced susceptibility artifacts in BOLD fMRI. *Magn Reson Med*. 2002;48:860-866.
21. Wilm BJ, Barmet C, Gross S, et al. Single-shot spiral imaging enabled by an expanded encoding model: demonstration in diffusion MRI. *Magn Reson Med*. 2017;77:83-91.
22. Kasper L, Engel M, Barmet C, et al. Rapid anatomical brain imaging using spiral acquisition and an expanded signal model. *Neuroimage*. 2018;168:88-100.
23. Aghaeifar A, Zhou J, Heule R, et al. A 32-channel multi-coil setup optimized for human brain shimming at 9.4 t. *Magn Reson Med*. 2020;83:749-764.
24. Pinho-Meneses B, Amadon A. A fieldmap-driven few-channel shim coil design for MRI of the human brain. *Phys Med Biol*. 2021;66:015001.
25. Pinho-Meneses B, Amadon A. Physical limits to human brain B0 shimming, engineering implications thereof hal-03210241v2 2021.
26. Andersson JL, Skare S, Ashburner J. How to correct susceptibility distortions in spin-echo echo-planar images: application to diffusion tensor imaging. *Neuroimage*. 2003;20:870-888.
27. Fritz L, Mulders J, Breman H. Comparison of EPI distortion correction methods at 3T and 7T. In Proceedings of the Annual Meeting of OHBM, Hamburg, Germany, 2014.
28. Noll DC. Multishot rosette trajectories for spectrally selective MR imaging. *IEEE Trans Med Imaging*. 1997;16:372-377.
29. Noll DC, Meyer CH, Pauly JM, Nishimura DG, Macovski A. A homogeneity correction method for magnetic resonance imaging with time-varying gradients. *IEEE Trans Med Imaging*. 1991;10:629-637.
30. Man L-C, Pauly JM, Macovski A. Multifrequency interpolation for fast off-resonance correction. *Magn Reson Med*. 1997;37:785-792.
31. Sutton BP, Noll DC, Fessler JA. Fast, iterative image reconstruction for MRI in the presence of field inhomogeneities. *IEEE Trans Med Imaging*. 2003;22:178-188.
32. Fessler JA, Lee S, Olafsson VT, Shi HR, Noll DC. Toeplitz-based iterative image reconstruction for MRI with correction for magnetic field inhomogeneity. *IEEE Trans Signal Process*. 2005;53:3393-3402.
33. Ostenson J, Robison RK, Zwart NR, Welch EB. Multi-frequency interpolation in spiral magnetic resonance fingerprinting for correction of off-resonance blurring. *Magn Reson Imaging*. 2017;41:63-72.
34. Man L-C, Pauly JM, Macovski A. Improved automatic off-resonance correction without a field map in spiral imaging. *Magn Reson Med*. 1997;37:906-913.
35. Sutton BP, Noll DC, Fessler JA. Dynamic field map estimation using a spiral-in/spiral-out acquisition. *Magn Reson Med*. 2004;51:1194-1204.
36. Patzig F, Wilm B, Gross S, Brunner D, Pruessmann KP. Off-Resonance Self-Correction for Single-Shot Imaging. In Proceedings of the 28th Annual Meeting of ISMRM, Virtual; 2020:3400.
37. Patzig F, Wilm B, Pruessmann KP. Off-resonance self-correction by implicit B0-encoding. In Proceedings of the 29th Annual Meeting of ISMRM. Virtual; 2021:666.
38. Salomir R, de Senneville BD, Moonen CT. A fast calculation method for magnetic field inhomogeneity due to an arbitrary distribution of bulk susceptibility. *Concepts Magn Reson Part B: Magn Reson Eng*. 2003;19:26-34.
39. Lee S-K, Hwang S-H, Barg J-S, Yeo S-J. Rapid, theoretically artifact-free calculation of static magnetic field induced by voxelated susceptibility distribution in an arbitrary volume of interest. *Magn Reson Med*. 2018;80:2109-2121.
40. Eckstein K, Bachrata B, Hangel G, et al. Improved susceptibility weighted imaging at ultra-high field using bipolar multi-echo acquisition and optimized image processing: CLEAR-SWI. *Neuroimage*. 2021;237:118175.
41. Baron CA, Nishimura DG. B0 mapping using rewinding trajectories (BMART). *Magn Reson Med*. 2017;78:664-669.
42. Robinson S, Grabner G, Witoszynskij S, Trattng S. Combining phase images from multi-channel RF coils using 3D phase offset maps derived from a dual-echo scan. *Magn Reson Med*. 2011;65:1638-1648.

43. Kimmlingen R. Magnetic field gradients. *Magnetic Resonance Technology: Hardware and System Component Design*; Royal Society of Chemistry; 2016:208-263.
44. De Graaf RA. *In Vivo NMR Spectroscopy: Principles and Techniques*. John Wiley & Sons; 2019.
45. Roemer PB, Edelstein WA, Hayes CE, Souza SP, Mueller OM. The NMR phased array. *Magn Reson Med*. 1990;16:192-225.
46. Parker DL, Payne A, Todd N, Hadley JR. Phase reconstruction from multiple coil data using a virtual reference coil. *Magn Reson Med*. 2014;72:563-569.
47. Walsh DO, Gmitro AF, Marcellin MW. Adaptive reconstruction of phased array MR imagery. *Magn Reson Med*. 2000;43:682-690.
48. Inati SJ, Hansen MS, Kellman P. A Solution to the Phase Problem in Adaptive Coil Combination. In Proceedings of the 21st Annual Meeting of ISMRM, Salt Lake City, Utah, USA; 2013:2672.
49. Inati SJ, Hansen MS, Kellman P. A fast optimal method for coil sensitivity estimation and adaptive coil combination for complex images. In Proceedings of the 22nd Annual Meeting of ISMRM, Milan, Italy; 2014:4407.
50. Ghiglia DC, Romero LA. Robust two-dimensional weighted and unweighted phase unwrapping that uses fast transforms and iterative methods. *JOSA A*. 1994;11:107-117.
51. Herráez MA, Burton DR, Lalor MJ, Gdeisat MA. Fast two-dimensional phase-unwrapping algorithm based on sorting by reliability following a noncontinuous path. *Appl Opt*. 2002;41:7437-7444.
52. Schofield MA, Zhu Y. Fast phase unwrapping algorithm for interferometric applications. *Opt Lett*. 2003;28:1194-1196.
53. Dymerska B, Eckstein K, Bachrata B, et al. Phase unwrapping with a rapid opensource minimum spanning tree algorithm (ROMEIO). *Magn Reson Med*. 2021;85:2294-2308.
54. Doneva M. Mathematical models for magnetic resonance imaging reconstruction: an overview of the approaches, problems, and future research areas. *IEEE Signal Process Mag*. 2020;37:24-32.
55. Hunt BR. Matrix formulation of the reconstruction of phase values from phase differences. *J Opt Soc Am*. 1979;69:393-399.
56. Chung S, Kim D, Breton E, Axel L. Rapid B1+ mapping using a preconditioning RF pulse with TurboFLASH readout. *Magn Reson Med*. 2010;64:439-446.
57. Van Lier ALHMW, Brunner DO, Pruessmann KP, et al. B1 phase mapping at 7 T and its application for in vivo electrical conductivity mapping. *Magn Reson Med*. 2012;67:552-561.
58. Le Ster C, Mauconduit F, Mirkes C, et al. RF heating measurement using MR thermometry and field monitoring: methodological considerations and first in vivo results. *Magn Reson Med*. 2021;85:1282-1293.
59. Van de Moortele P-F, Pfeuffer J, Glover GH, Ugurbil K, Hu X. Respiration-induced B0 fluctuations and their spatial distribution in the human brain at 7 tesla. *Magn Reson Med*. 2002;47:888-895.
60. Robinson SD, Bredies K, Khabipova D, Dymerska B, Marques JP, Schweser F. An illustrated comparison of processing methods for MR phase imaging and QSM: combining array coil signals and phase unwrapping. *NMR Biomed*. 2017;30:e3601.
61. Vaidya M, Collins C, Sodickson D, Brown R, Wiggins G, Latanzi R. Dependence of B1- and B1+ field patterns of surface coils on the electrical properties of the sample and the MR operating frequency. *Concepts Magn Reson Part B: Magn Reson Eng*. 2016;46:25-40.
62. Brodsky EK, Klaers JL, Samsonov AA, Kijowski R, Block WF. Rapid measurement and correction of phase errors from B0 eddy currents: impact on image quality for non-Cartesian imaging. *Magn Reson Med*. 2013;69:509-515.
63. Hedley M, Yan H. Motion artifact suppression: a review of post-processing techniques. *Magn Reson Imaging*. 1992;10:627-635.
64. Welch EB, Manduca A, Grimm RC, Ward HA, Jack CR Jr. Spherical navigator echoes for full 3D rigid body motion measurement in MRI. *Magn Reson Med*. 2002;47:32-41.
65. Van Rossum G, Drake FL Jr. *Python Tutorial*. Centrum voor Wiskunde en Informatica; 1995.
66. Okuta R, Unno Y, Nishino D, Hido S, Loomis C. CuPy: A NumPy-Compatible Library for NVIDIA GPU Calculations. In Proceedings of Workshop on Machine Learning Systems (LEARNINGSYS) in the Thirty-First Annual Conference on Neural Information Processing Systems (NIPS), Long Beach, CA, USA; 2017.
67. Baldi A, Bertolino F, Ginesu F. Phase unwrapping algorithms: a comparison. *Interferometry in Speckle Light*. Springer; 2000:483-490.
68. Van der Walt S, Schönberger JL, Nunez-Iglesias J, et al. Scikit-image: image processing in python. *PeerJ*. 2014;2:e453.
69. Bezanson J, Edelman A, Karpinski S, Shah VB. Julia: a fresh approach to numerical computing. *SIAM Rev*. 2017;59:65-98.
70. Metere R, Möller HE. PyMRT and DCMPI: Two new Python packages for MRI data analysis. In Proceedings of the 25th Annual Meeting of ISMRM, Honolulu, HI, USA; 2017:3816.
71. Buehrer M, Pruessmann KP, Boesiger P, Kozerke S. Array compression for MRI with large coil arrays. *Magn Reson Med*. 2007;57:1131-1139.
72. Knoll F, Schwarzl A, Diwokoy C, Sodickson DK. gnuNUFFT-an open source GPU library for 3D regridding with direct Matlab interface. In Proceedings of the 22nd Annual Meeting of ISMRM, Milan, Italy; 2014:4297.
73. Pipe JG, Menon P. Sampling density compensation in MRI: rationale and an iterative numerical solution. *Magn Reson Med*. 1999;41:179-186.
74. Farrens S, Grigis A, El Gueddari L, et al. PySAP: python sparse data analysis package for multidisciplinary image processing. *Astron Comput*. 2020;32:100402.
75. El Gueddari L, Chaithya G, Ramzi Z, et al. PySAP-MRI: a Python package for MR image reconstruction. In ISMRM Workshop on Data Sampling and Image Reconstruction, Sheffield, UK; 2020.
76. El Gueddari L, Lazarus C, Carrié H, Vignaud A, Ciuciu P. Self-calibrating nonlinear reconstruction algorithms for variable density sampling and parallel reception MRI. *2018 IEEE 10th Sensor Array and Multichannel Signal Processing Workshop (SAM)*. IEEE; 2018:415-419.
77. Dubovan P, Kasper L, Uludag K, Baron C. On the impact of B0 map resolution and undersampling on reconstructions using expanded encoding models. In Proceedings of the 29th Annual Meeting of ISMRM, Virtual; 2021:892.
78. Zhao Z, Zhang H, Ma C, Fan C, Zhao H. Comparative study of phase unwrapping algorithms based on solving the Poisson equation. *Meas Sci Technol*. 2020;31:065004.

SUPPORTING INFORMATION

Additional supporting information may be found in the online version of the article at the publisher's website.

Section S1 Phase contributions from eddy currents. Additional experiment proposed to estimate the phase contributions of eddy currents during the main experiments.

Section S2 Coil combination. Detail of the diverse modification of the ACC algorithm used during estimations and reconstructions.

Section S3 Phase unwrapping. Detail of the diverse modification of the phase unwrapping algorithm used during estimations and reconstructions.

Section S4 Image reconstruction and ΔB_0 correction. Detailed reconstruction and correction techniques used for both estimation and reconstruction pipelines.

Section S5 Convergence of the ΔB_0 estimation. Additional reconstructions and details showing the empirical convergence of the estimation algorithm.

Section S6 ΔB_0 map resolution impact on estimation and correction. Additional experiment proposed to show the impact of reduced field map resolution post-estimation on correction quality.

Section S7 Additional quantitative results on ΔB_0 estimation and correction. Diverse additional results proposed to complete the main discussion.

Figure S1 Phase contributions from the B_e field on oil phantom. The contribution from eddy currents was estimated from phase maps in 4 different contexts: without (A) or with (B) a pre-pulse gradient of 10 mT/m, and with either a body coil array (1) or a 64-channel head/neck coil array (2). The voxels of minimum (blue arrows) and maximum (red arrows) values of the phase ϕ_{B_e} are automatically pointed out

Figure S2 Evolution of 4 ΔB_0 map estimations and corresponding corrections over 15 steps. The ΔB_0 estimation (A B) and consequent correction (C,D) are monitored during the estimation process over 15 steps, using an average L2 norm and SSIM score, respectively. The evolution is first observed by comparing each step with the fixed initial steps (A,C), corresponding to 0-filled maps for the estimation (A) and the non-corrected volume for the correction (C). The relative progression is shown by comparing each step with the next one (B,D). The results are displayed for

each volunteer and each score, and a vertical dotted line shows the number of steps used in our proposition.

Figure S3 Comparison of different volumes corrected using multiple ΔB_0 map resolutions. The ΔB_0 map estimated with a resolution of 0.6 mm isotropic from acquisition 3 and used to produce the 3D SWI volume (A) was downsampled to 4 mm, 2 mm, and 1 mm to obtain on row (1) the corrected volumes (C), (D) and (E), respectively. The original volume without correction (B) is shown for reference. The absolute value of the differences between (B-E) and (A) are displayed on row (2), multiplied by a factor 5.

Figure S4 Phase images from corrected volumes with or without ΔB_0 map filtering. The impact of filtering during the ΔB_0 estimation is shown over the 5-channel 1-step volumes obtained during the estimation process for volunteer 3.

Figure S5 Bland-Altman plots comparing the estimated and acquired ΔB_0 maps. For each volunteer (1 to 4), the differences between estimated and acquired ΔB_0 maps are shown according to the average between both values, for only 1 every 10 voxels for clarity purpose. The average and ± 1.96 standard deviation (SD) of the differences are shown with plain and dotted red lines, respectively.

Table S1 Scores for different SWI volumes corrected using multiple ΔB_0 map resolutions. Different scores were computed to compare the SWI volume obtained from the ΔB_0 map estimated with a resolution of 0.6 mm isotropic from acquisition 3 and the SWI volumes obtained by downsampling the same map to 4 mm, 2 mm, and 1 mm.

Table S2 Scores for the SWI volumes produced using estimated ΔB_0 maps. Different scores were computed for each volunteer to compare the corrected SWI volume obtained from the estimated ΔB_0 map, as described in the main experiments, and the SWI volumes without correction and corrected using an acquired ΔB_0 map.

How to cite this article: Daval-Fr erot G, Massire A, Mailhe B, Nadar M, Vignaud A, Ciuciu P. Iterative static field map estimation for off-resonance correction in non-Cartesian susceptibility weighted imaging. *Magn Reson Med.* 2022;88:1592-1607. doi: 10.1002/mrm.29297